Check for updates

Ru$_x$Se@MoS$_2$ hybrid as a highly efficient electrocatalyst toward hydrogen evolution reaction†

Qi Chen,[ab] Kefeng Wang, [iD] *[b] Jingjing Qin,[b] Songzhu Wang,[b] Wei Wei,[b] Jingge Wang,[c] Qi Shen,[d] Peng Qu[b] and Daosheng Liu*[a]

Alkaline hydrogen evolution reaction (HER) requires highly efficient and stable catalytic materials, the engineering of which needs overall consideration of the water dissociation process as well as the intermediate hydrogen adsorption process. Herein, a Ru$_x$Se@MoS$_2$ hybrid catalyst was synthesized by the decoration of MoS$_2$ with Ru$_x$Se nanoparticles through a two-step hydrothermal reaction. Due to the bifunctionality mechanism in which Ru promotes the water dissociation and the nearby Se atoms, unsaturated Mo and/or S atoms act as active sites for the intermediate hydrogen adsorption, the hybrid catalyst exhibits an exceptional HER performance in basic media with a rather low overpotential of 45 mV at a current density of 10 mA cm^{-2} and a small Tafel slope of 42.9 mV dec^{-1}. The synergetic effect between Ru$_x$Se and MoS$_2$ not only enables more catalytically active sites, but also increases the inherent conductivity of the hybrid catalyst, leading to more favorable HER kinetics under both alkaline and acidic conditions. As a result, Ru$_x$Se@MoS$_2$ also demonstrates an enhanced catalytic activity toward HER in 0.5 M H$_2$SO$_4$ in comparison with pure Ru$_x$Se and MoS$_2$, which requires an overpotential of 120 mV to deliver a 10 mA cm^{-2} current density and gives a Tafel slope of 72.2 mV dec^{-1}. In addition, the hybrid electrocatalyst also exhibits superior electrochemical stability during the long-term HER process in both acidic media and alkaline media.

1. Introduction

The gradual depletion of traditional fossil fuels forces us to search for renewable energies such as solar energy, wind energy, hydrogen energy, *etc.* Among all these renewable energies, hydrogen energy is deemed as the potential alternative to fossil fuels in future due to its various favorable features including carbon-free footprint, high mass-energy density and simple production methodologies. Water electrolysis coupling with renewable energies is considered as one of the most appealing approaches for large-scale hydrogen generation.[1] Due to the sluggish reaction kinetics at the electrode interface, an overpotential is required to drive the HER and the oxygen evolution reaction (OER).[2] Platinum-based materials and Ru, Ir-based materials are the state-of-the-art HER and OER catalysts, respectively.[3,4] Unfortunately, their scarcity, unaffordable high cost and inferior durability greatly impede the wide application of such catalysts in industrial water-splitting technology. Therefore, it is of paramount importance to develop low-cost and highly efficient electrocatalysts with abundant sources. Relentless efforts have been devoted to exploring highly efficient electrocatalysts with abundant and low-cost transition metal-based materials.[3,5-8] However, the electrocatalytic activity of these earth-abundant materials is still far from satisfactory compared with that of Pt-based catalysts. Combining the abundant transition metal-based materials with a low dosage of noble metal could be a promising approach to design highly efficient and low-cost electrocatalysts for HER.

MoS$_2$ is considered as the most promising alternative to Pt for electrocatalytic hydrogen evolution reaction due to its low cost, abundant source as well as the excellent electrochemical stability. However, the catalytic activity of MoS$_2$ is greatly limited by the insufficient active sites and inherent poor conductivity. To address these issues, various strategies have been explored to boost the catalytic performance of MoS$_2$-based materials in acidic electrolytes, including morphology and phase control,[9-16] defect engineering,[17-19] regulating the

[a]College of Chemistry, Chemical Engineering and Environmental Engineering, Liaoning Shihua University, Fushun 113001, Liaoning, China. E-mail: dsliu05@126.com

[b]Henan Engineering Center of New Energy Battery Materials, Henan Key Laboratory of Biomolecular Recognition and Sensing, College of Chemistry and Chemical Engineering, Shangqiu Normal University, Shangqiu 476000, Henan, China. E-mail: wangkf2007@163.com

[c]School of Physics and Engineering, Henan University of Science and Technology, Luoyang 471023, China

[d]College of Chemistry and Molecular Engineering, Zhengzhou University, Zhengzhou 450001, China

electronic structures by heteroatom doping,[20–25] engineering heterostructures with conducting carbonaceous materials and other transition metal-based materials.[26–32] Through these intrinsic and extrinsic modifications, the activities of some MoS_2-based composites in acidic electrolytes have been approaching those of Pt-based materials. However, due to the high energy barrier to initiate water dissociation for MoS_2, the HER kinetics in alkaline media is sluggish. In order to surmount this obstacle to accelerate the HER process in alkaline media, water dissociation promoters have been integrated for designing heterostructures.[29,33–35]

Among all the precious metals, Ru with a price 1/25 that of Pt possesses the best water dissociation ability. In this regard, PtRu demonstrates the best electrocatalytic performance for methanol oxidation reaction. The superior catalytic performance is due to the synergetic effect in which Ru promotes the water electro-oxidation to supply oxygen-containing species and Pt serves as active sites for the oxidation of poisonous CO.[36,37] However, as the adsorption of oxygenated species on Ru is too strong, Ru has demonstrated the relative lower HER activities under both acidic and basic conditions when compared with other noble metals such as Ir and Pt.[38] By forming phosphides (RuP or RuP_2) or integration with transition-metal compound and N and/or P-doped carbon materials, the electronic structure of Ru would be well tuned, leading to less strong adsorption of oxygenated species. As a result, RuP_x alone or encapsulated in carbon nanomaterials,[39–45] carbonaceous materials-supported Ru nanoparticles or nanoclusters,[46–55] RuS_2/S-doped graphene composite,[56] NiCoP@Ru,[57] Ru/MoS$_2$,[58] Ru/Cu-doped RuO_2,[59] Ru/CoP,[60] et al. have been investigated as highly efficient HER electrocatalysts in alkaline electrolytes. Nevertheless, little attention has been paid to the potential application of ruthenium selenides (Ru_xSe), though other metal selenides have been widely utilized in catalysis.[61–64] As Se centres in several transition metal selenides have been proved to possess favorable free energies for hydrogen adsorption,[65,66] Ru_xSe is expected to be a potential highly efficient HER catalyst in alkaline electrolytes in which Ru could facilitate the water cleavage process to generate hydrogen intermediates. In a more recent study, we have demonstrated that $Ru_{0.33}Se$ nanoparticles-decorated TiO_2 nanotube arrays ($Ru_{0.33}Se@TNA$) could be utilized as a highly efficient alkaline HER catalyst with an overpotential of only 57 mV to deliver a current density of 10 mA cm^{-2} and a Tafel slope of 50 mV dec^{-1}. More importantly, the current density of $Ru_{0.33}Se@TNA$ exceeds that of 20% Pt/C catalyst at higher overpotentials.[67] However, the active sites for the intermediate hydrogen adsorption in Ru_xSe is limited and the free energies on Se sites are far less favorable than those on the Mo-edge sites in MoS_2. Furthermore, MoS_2 nanosheets with an ultrahigh specific area enable the engineering of hybrid nanomaterials with other materials. A large variety of materials have been integrated with MoS_2 nanosheets to fabricate hybrid catalysts for water electrolysis, and the resultant hybrids usually exhibit enhanced catalytic activities owing to the synergetic effect between the building blocks.[32,34,35,68] In this regard, a hybrid catalyst combining MoS_2 and Ru_xSe would demonstrate an impressive electrocatalytic performance toward HER

in alkaline electrolytes owing to the bifunctionality mechanism in which Ru promotes the water dissociation and the nearby Se atoms, unsaturated Mo and/or S atoms act as active sites for the intermediate hydrogen adsorption.

In the present work, $Ru_xSe@MoS_2$ hybrid catalyst was fabricated by integrating Ru_xSe nanoparticles with MoS_2 nanosheets. Owing to the synergetic effect between Ru_xSe and MoS_2, the hybrid catalyst demonstrates a superb electrocatalytic activity toward HER in basic media with an overpotential of only 45 mV to generate a current density of 10 mA cm^{-2}, a small Tafel slope of 42.9 mV dec^{-1} and an extraordinary electrochemical stability. Furthermore, the hybrid catalyst also shows an enhanced catalytic activity for HER in acidic media in comparison with MoS_2 and Ru_xSe.

2. Results and discussion

The crystal structure of the hybrid catalyst was characterized using an X-ray diffractometer (XRD). Fig. 1 shows the XRD pattern of $Ru_xSe@MoS_2$ grown on carbon fiber paper. The diffraction peak around 26° is originated from the carbon fiber paper substrate. The peaks at $2\theta = 14.5°$, 32.7° and 58.3° could be well indexed to the (002), (100) and (110) planes of the standard XRD pattern of hexagonal $2H–Mo_2S$ (JCPDS card no. 37-1492), respectively. It should be noted that $Ru_xSe@MoS_2$ almost exhibits the same diffraction pattern as the pure MoS_2 grown on the carbon fiber paper, suggesting the negligible effect of Ru_xSe nanoparticle deposition on the crystal structure of MoS_2. However, due to the small loading as well as the low crystallinity, the diffraction peaks assigned to the deposited Ru_xSe nanoparticles could not be detected. To further determine the crystal characteristics of Ru_xSe nanoparticles, the powder product in the hydrothermal reaction for the synthesis of $Ru_xSe@MoS_2$ hybrid was also collected for XRD measurement. As shown in Fig. 1, Ru_xSe powder exhibits two broad
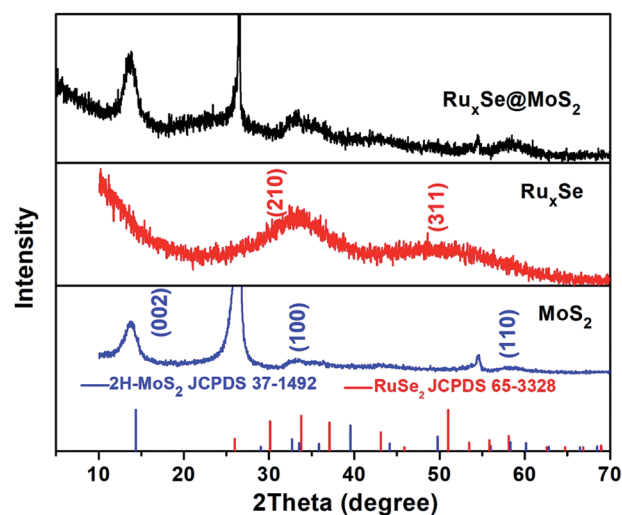

Fig. 1 XRD patterns of MoS_2, Ru_xSe and $Ru_xSe@MoS_2$, and the standard patterns of $2H–MoS_2$ (JCPDS No. 37-1492) and $RuSe_2$ (JCPDS No. 65-3328).

diffraction peaks around $2\theta = 33.8°$ and $51.0°$ assigned to crystalline $RuSe_2$ (JCPDS No. 65-3328), indicating the low crystallinity of Ru_xSe nanoparticles. It is worth to be pointed out that the crystallinity of Ru_xSe powder could be greatly enhanced by calcination at 400 °C (Fig. S1, ESI†).

The microstructure of the pure MoS_2 and $Ru_xSe@MoS_2$ hybrid was investigated by scanning electron microscopy (SEM). As demonstrated in Fig. 2a and S2 (ESI†) for the morphology of MoS_2 grown on the carbon fiber paper, the carbon fibers are covered with vertically aligned MoS_2 sheets with a thickness of 20 nm, and hierarchical micro-flowers composed of interconnected MoS_2 nanosheets with an average diameter of 2.5 μm are also formed on the top of MoS_2 sheet layer. After integration with Ru_xSe via a further hydrothermal reaction with $RuCl_3$ and Se powder as the Ru source and Se source, respectively, Ru_xSe nanoparticles were uniformly anchored on the vertically aligned nanosheets as well as the petals of the micro-flowers (Fig. 2b). It

could be obviously noted that all the nanosheets preserve the original alignment, but the surface becomes rough with a thickness increasing to about 30 nm. Energy-dispersive X-ray spectroscopy (EDX) mapping images (Fig. 2c) suggest the uniform distribution of Mo, S, Ru and Se elements throughout the whole film, further confirming the homogeneous distribution of Ru_xSe nanoparticles on MoS_2 nanosheets. The atomic ratio of Ru to Mo in the $Ru_xSe@MoS_2$ hybrid is determined to be 2.95% according to the EDX spectrum (Fig. S3, ESI†), indicating a rather low usage of Ru for the fabrication of the hybrid catalysts.

Transmission electron microscopy (TEM) and high-resolution TEM (HRTEM) images were recorded to further investigate the structural detail of the samples. As shown in Fig. 2d, Ru_xSe nanoparticles with a diameter range of 20–30 nm are highly dispersed on MoS_2 nanosheets without any obvious agglomerates. However, the pure Ru_xSe synthesized under the
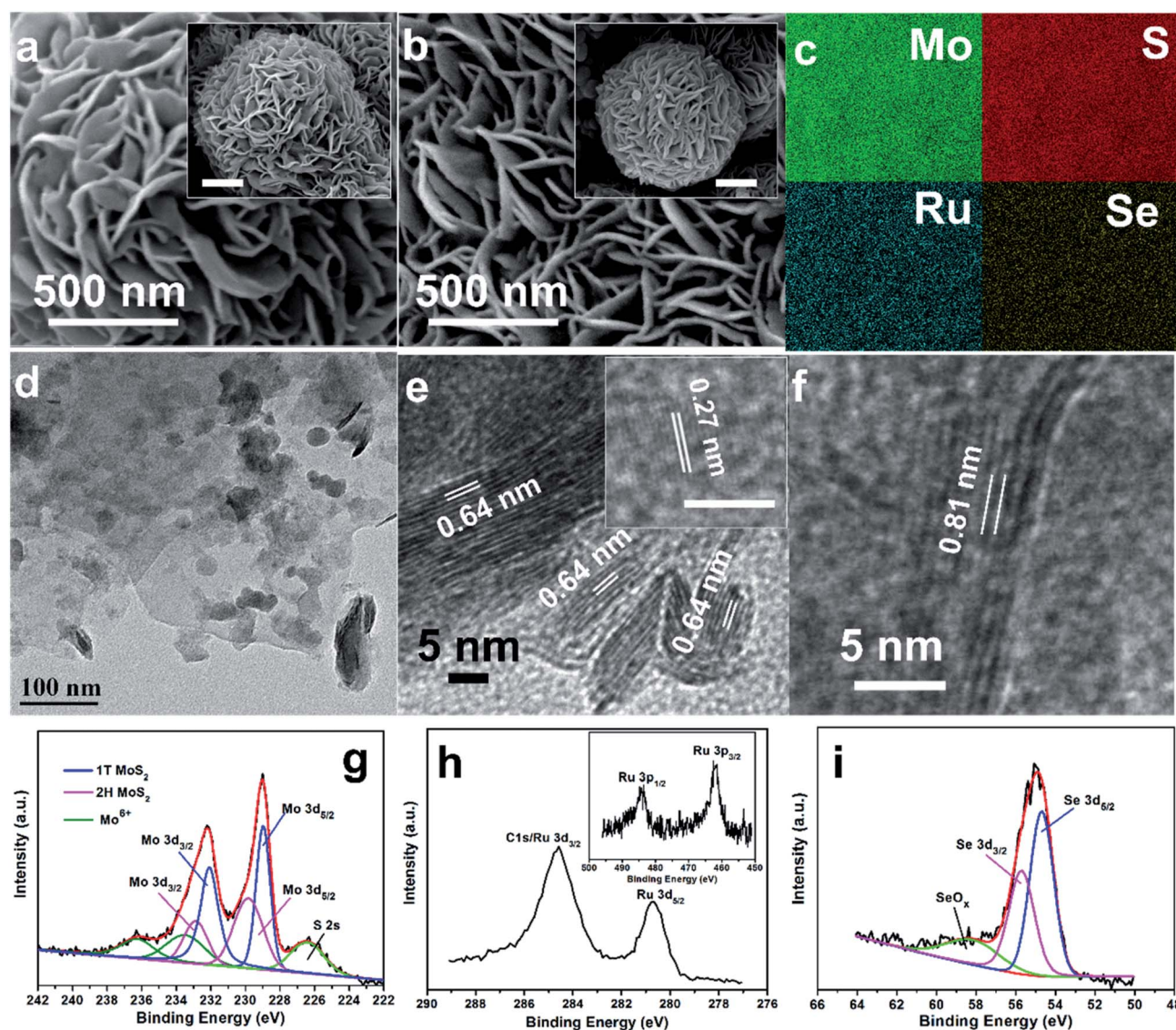

Fig. 2 (a and b) SEM images of MoS_2 and $Ru_xSe@MoS_2$. The scale bar in the insets is 500 nm. (c) EDX mappings of $Ru_xSe@MoS_2$. (d) TEM image of $Ru_xSe@MoS_2$. (e and f) HRTEM images of $Ru_xSe@MoS_2$. (g–i) High resolution XPS spectra of Mo 3d, Ru 3d (inset: Ru 3p) and Se 3d.

same conditions exhibits severe particle aggregation revealed by TEM image shown in Fig. S4 (ESI†). Therefore, MoS_2 nanosheets with a large specific area could facilitate the homogeneous distribution of Ru_xSe nanoparticles, enabling more exposed active sites for catalytic reactions. In the HRTEM images displayed in Fig. 2e and S5,† the lattice fringes with spaces of 0.64 nm and 0.27 nm could be attributed to the (002) and (100) crystallographic planes of $2H–MoS_2$, respectively. Additionally, the lattice fringe with a larger interplanar space of 0.81 nm in Fig. 2f corresponds to the (002) plane of $1T-MoS_2$,[14] indicating a mixture phase of MoS_2 in the $Ru_xSe@MoS_2$ hybrid.

X-ray photoelectron spectroscopy (XPS) was carried out to further verify the valence states of different elements in $Ru_xSe@MoS_2$. In the high-resolution Mo 3d spectrum (Fig. 2g), the peaks around 228.7 eV and 231.8 eV could be assigned to Mo $3d_{5/2}$ and Mo $3d_{3/2}$ of $1T-MoS_2$, respectively. Another two peaks located at binding energies of 229.6 eV and 232.6 eV are attributed to Mo $3d_{5/2}$ and Mo $3d_{3/2}$ of $2H–MoS_2$, respectively.[13,14,69,70] The last two weak peaks around 233.3 eV and 236.1 eV are ascribed to Mo $3d_{5/2}$ (Mo^{6+}) and Mo $3d_{3/2}$ (Mo^{6+}), suggesting partial oxidation of the sample on the surface. Fig. 2h displays the high-resolution Ru 3d spectrum. Two peaks belonging to Ru $3d_{5/2}$ and Ru $3d_{3/2}$ are observed at the binding energies of 280.6 eV and 284.6 eV. Notably, the peak intensity of Ru $3d_{3/2}$ is much stronger than that of Ru $3d_{5/2}$ due to the coexist of C 1s peaks in the Ru 3d region.[44] Accordingly, the characteristic peaks assigned to Ru $3p_{3/2}$ and Ru $3d_{1/2}$ are detected at 462.0 eV and 484.7 eV in the high resolution Ru 3p spectrum (Fig. 2h inset).[44] For Se 3d spectrum (Fig. 2i), the doublet around 54.4 eV and 55.7 eV could be attributed to Se $3d_{3/2}$ and Se $3d_{5/2}$, respectively.[65]

$Ru_xSe@MoS_2$ was utilized as catalyst for hydrogen evolution reaction in 1.0 M KOH solution, and the HER activity was evaluated by measuring polarization curves using a standard three-electrode configuration. $Ru_xSe@MoS_2$ grown on the carbon fiber paper with dimensions of 1 cm × 1 cm was directly used as the working electrode, the graphite rod and HgO/Hg electrode were employed as the counter electrode and reference electrode, respectively. For comparison, the HER activities of the pristine MoS_2, Ru_xSe and commercial 20% Pt/C catalysts were also measured under the same conditions. The HER activities of different catalysts were characterized by IR-corrected polarization curves shown in Fig. 3a. It could be obviously seen that MoS_2 exhibits a poor HER activity with a high overpotential of 177 mV to acquire a current density of 10 mA cm^{-2}. Ru_xSe displays a higher HER activity with a smaller overpotential of 119 mV to deliver the same current density. Commercial 20% Pt/C catalyst demonstrates a better HER performance than both MoS_2 and Ru_xSe, which could achieve a current density of 10 mA cm^{-2} at an overpotential of 98.0 mV. For $Ru_xSe@MoS_2$ hybrid, the HER performance dramatically enhanced, and the overpotential to afford the same current density for $Ru_{0.33}Se@MoS_2$ reduces to 45 mV, just 132 mV and 74 mV lower than those of MoS_2 and Ru_xSe, respectively. More importantly, the overpotential at 10 mA cm^{-2} for $Ru_xSe@MoS_2$ hybrid catalyst is also among the best reported levels so far for MoS_2-based HER catalysts in basic electrolyte (Table S1, ESI†).

Tafel slope could be used to provide further insight into the intrinsic HER kinetics of the electrocatalysts. A smaller Tafel slope implies a faster current increase with a specified over-potential change. Fig. 4b shows the corresponding Tafel plots transferred from the polarization curves. MoS_2 exhibits a Tafel slope of 101.1 mV dec^{-1}, almost the same as that of Ru_xSe (107.3 mV dec^{-1}). After hybridization, $Ru_xSe@MoS_2$ demonstrates an obviously decreased Tafel slope of 42.9 mV dec^{-1} comparable to the that of the commercial 20% Pt/C catalyst (34.2 mV dec^{-1}), indicating a dramatically improved HER kinetics. The Tafel slope of $Ru_xSe@MoS_2$ suggests a Volmer–Heyrovsky mechanism during the HER process and the hydrogen desorption is the rate-limiting step. Moreover, we also compared the Tafel slope of $Ru_xSe@MoS_2$ with those of MoS_2-based HER catalysts in basic media (Table S1, ESI†), further demonstrating the superb electrocatalytic HER kinetics of the hybrid catalyst.

In order to further evaluate the inherent HER activity, the exchange current density (J_0) at the thermodynamic redox potential ($\eta = 0$) was obtained by extrapolating the horizontal intercept of the linear region of the Tafel plot. Accordingly, our hybrid catalyst gives a J_0 of 0.91 mA cm^{-2}, far larger than the values for MoS_2 (0.19 mA cm^{-2}) and Ru_xSe (0.78 mA cm^{-2}). The highest J_0 for $Ru_xSe@MoS_2$ implies the most favorable electron transfer kinetics under zero overpotential, leading to the superior electrocatalytic performance toward HER in alkaline media. In addition, the exchange current density for $Ru_xSe@MoS_2$ is also comparable or larger than the values for those reported MoS_2-based alkaline HER catalysts.[29,33]

To validate the superior charge-transfer kinetics of $Ru_xSe@MoS_2$ under HER-operating conditions, electrochemical impedance spectroscopy (EIS) measurements were carried out under an overpotential of −200 mV. As shown in Fig. 3c, the semicircle in the low-frequency region of the Nyquist plot represents the charge- transfer resistance between the catalysts and the substrates. The smaller the charge- transfer resistance (R_{ct}) is, the more favorable charge transfer kinetics will be. Compared with Ru_xSe (3.93 Ω) and MoS_2 (27.8 Ω) electrodes, $Ru_xSe@MoS_2$ electrode exhibits a substantially lower R_{ct} of 1.16 Ω, indicating a superior inherent conductivity which is probably induced by the synergy between Ru_xSe and MoS_2. Therefore, the hybrid affords a more rapid electron transport process and a faster HER kinetics.

The exceptional HER activity of $Ru_xSe@MoS_2$ may stem from the synergetic coupling effect of MoS_2 nanosheets and Ru_xSe nanoparticles: (i) Ru promotes the dissociation of H_2O into H_{ads} and OH^-. While Se sites and/or the edge sites of MoS_2 with a moderate hydrogen absorption energy are favorable for speeding up the hydrogen generation kinetics. (ii) The homogeneous dispersion of Ru_xSe nanoparticles on MoS_2 nanosheets greatly suppresses particle aggregation, thus ensuring more exposed active sites and enhancing the utilization efficiency of Ru_xSe. (iii) The hybridization greatly improves catalyst conductivity and enhances the charge transfer efficiency, thus accelerating the electrocatalytic process.

Electrochemical durability of the hybrid catalyst is assessed by a long-term cycling test. Fig. 3d compares the polarization
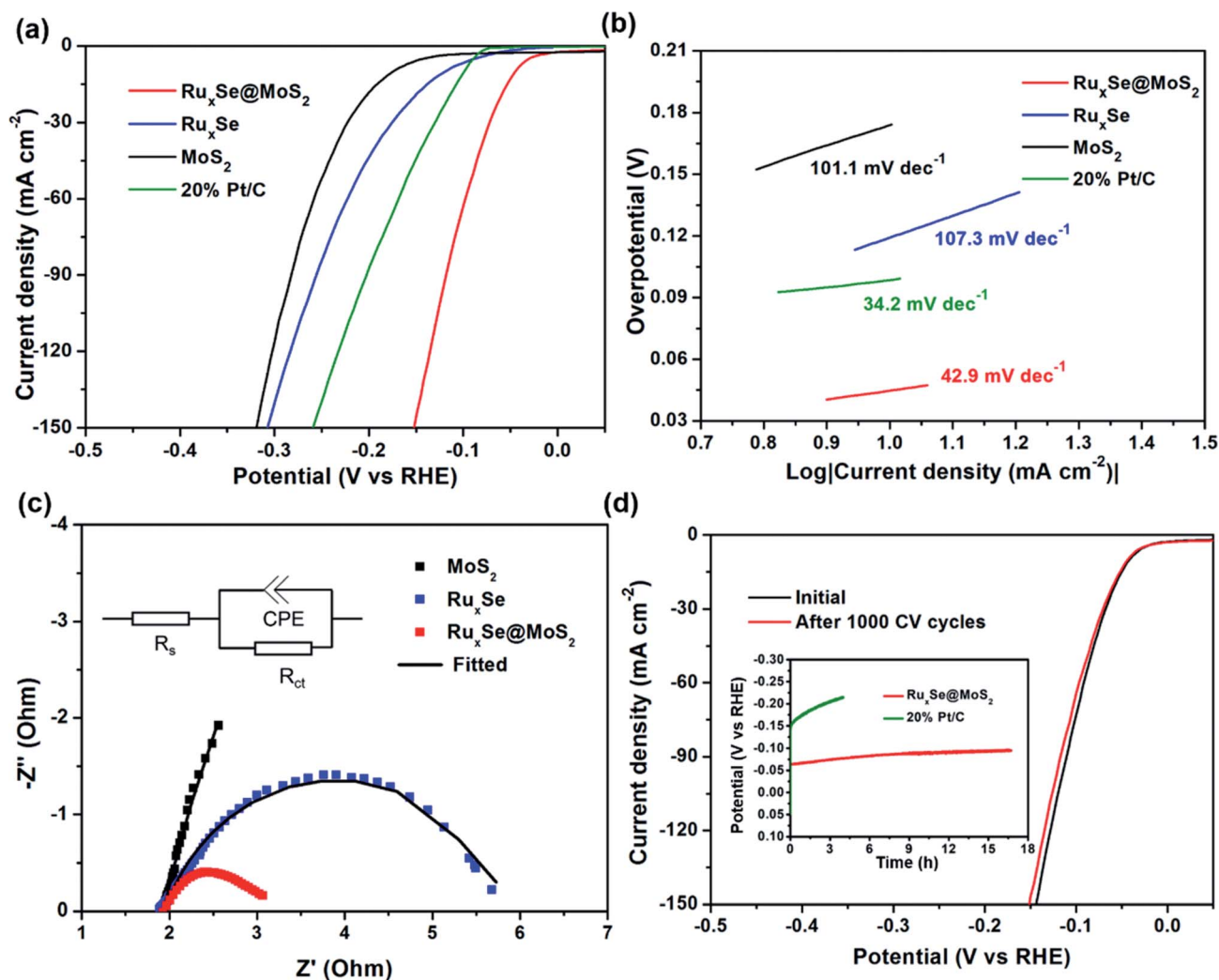
Fig. 3 (a) Polarization curves and (b) the corresponding Tafel plots of $Ru_xSe@MoS_2$, Ru_xSe, MoS_2 and commercial 20% Pt/C catalysts recorded in a N_2-saturated 1 M KOH aqueous solution with a scan rate of 2 mV s^{-1}. (c) EIS Nyquist plots recorded at an overpotential of −200 mV and the corresponding equivalent circuit model (inset). (d) Polarization curves of $Ru_xSe@MoS_2$ measured before and after continuous CV tests and the long-term stability of $Ru_xSe@MoS_2$ and commercial 20% Pt/C determined by chronopotentiometry at a current density of −20 mA cm^{-2} (inset).

curves recorded before and after 1000 cyclic voltammetry (CV) cycles. The almost overlapped curves indicate a highly electrochemical stability of the hybrid catalyst during the long-term continuous HER test. Moreover, we also conducted the long-term HER test under a constant current density of –20 mA cm^{-2}, and the corresponding time-dependent potential change was recorded in Fig. 3d (inset). Obviously, the potential shows an insignificant variation during a 16 h test, further evidencing the superb stability of our hybrid catalyst. Moreover, the morphology $Ru_xSe@MoS_2$ hybrid after the long-term stability test was also investigated by SEM and TEM. As shown in Fig. S6 and S7 (ESI†), there is no significant change in the microstructure of $Ru_xSe@MoS_2$, indicating a high structural stability of $Ru_xSe@MoS_2$ during the continuous HER test. Unfortunately, commercial 20% Pt/C catalyst exhibits a rather poor long-term stability for HER test in basic media. As shown in the Fig. 4d (inset), the potential at −20 mA cm^{-2} reduced

from −0.15 V to −0.22 V during only a 4 h continuous HER operation.

Next, we further examined the HER performance of $Ru_xSe@MoS_2$ in a 0.5 M H_2SO_4 electrolyte. Linear sweep voltammetry (LSV) curves of different catalysts were recorded using a three-electrode setup with an Ag/AgCl (saturated KCl solution) electrode as the reference electrode. As expected, commercial 20% Pt/C catalyst shows a superb HER performance with a small overpotential of 47.1 mV to give a 10 mA cm^{-2} current density and a Tafel slope of 43.6 mV dec^{-1}. $Ru_xSe@MoS_2$ hybrid catalyst requires an overpotential of 120 mV to achieve a current density of 10 mA cm^{-2}, much smaller than those for pure MoS_2 (209 mV) and Ru_xSe (169 mV), respectively. The Tafel slopes of different catalysts were also calculated according to the LSV curves in order to probe the HER kinetics in acidic media. Compared with the Tafel slopes obtained in alkaline media, both MoS_2 and Ru_xSe demonstrate smaller Tafel slopes under acidic conditions, suggesting faster HER kinetics in acidic
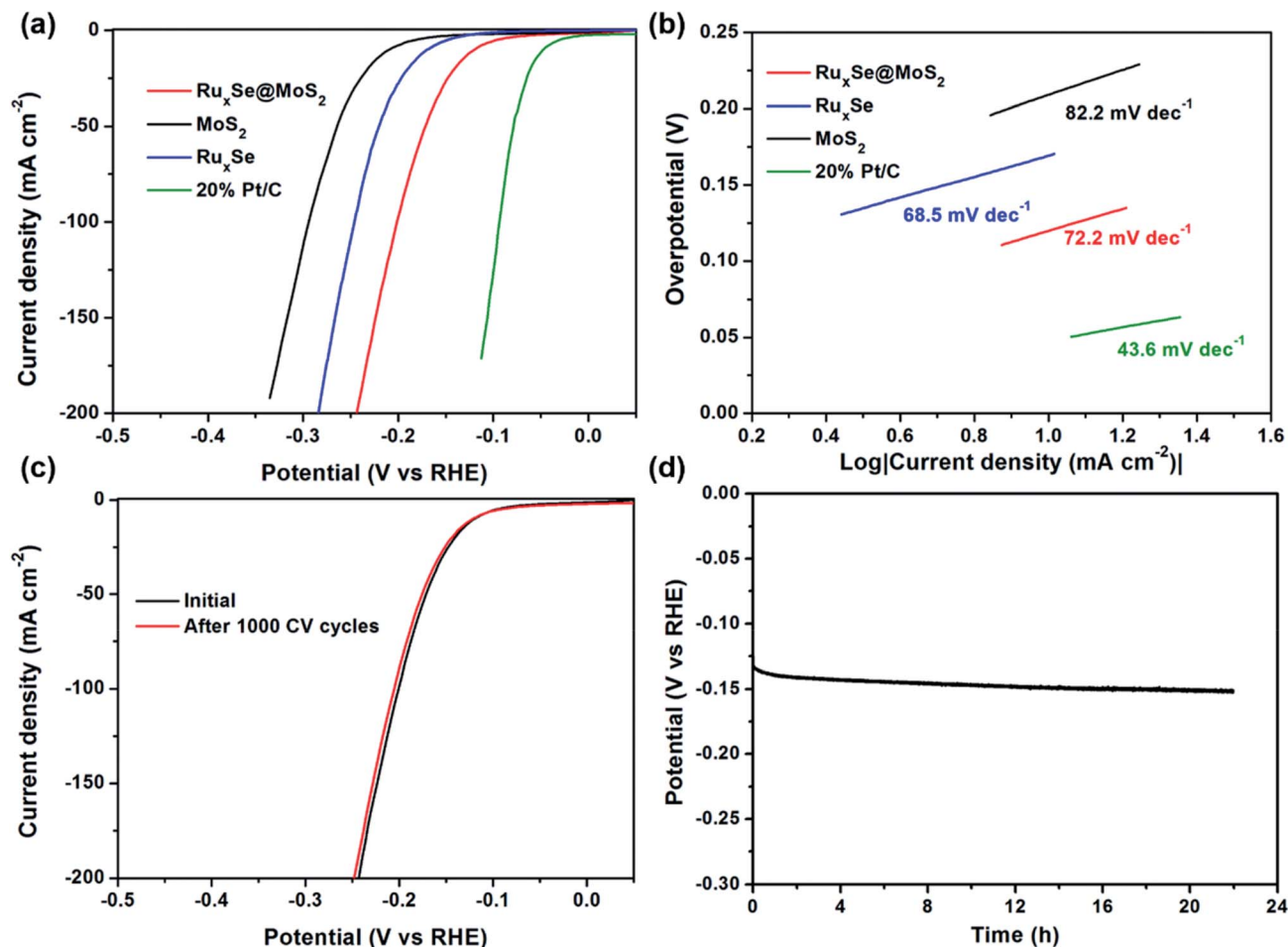
Fig. 4 (a) Polarization curves of $Ru_xSe@MoS_2$, Ru_xSe, MoS_2 and commercial 20% Pt/C catalysts recorded in a N_2-saturated 0.5 M H_2SO_4 aqueous solution. (b) The corresponding Tafel plots. (c) Polarization curves of $Ru_xSe@MoS_2$ before and after 1000 CV cycles. (d) Chronopotentiometric curve recorded at a constant current density of -20 mA cm^{-2}.

media. However, $Ru_xSe@MoS_2$ hybrid catalyst showed a larger Tafel slope of 72.2 mV dec^{-1}, indicating a decreased HER kinetics under acidic conditions in comparison with that in alkaline situation, as acidic HER process is predominated by the intermediate hydrogen adsorption kinetics without the water dissociation process which would be accelerated by Ru in alkaline media. The exchange current densities for different catalysts in 0.5 M H_2SO_4 were also calculated. $Ru_xSe@MoS_2$ shows a larger J_0 value of 0.22 mA cm^{-2} than Ru_xSe (0.034 mA cm^{-2}) and MoS_2 (0.029 mA cm^{-2}), further corroborating the faster electron transfer kinetics in the hybrid catalyst.

The stability of the hybrid catalyst in acidic electrolyte was also assessed by 1000 cycles of CV scanning at a scan rate of 100 mV s^{-1}. As displayed in Fig. 4c, the polarization curve recorded after continuous CV scanning is almost identical to the initial one, indicating an ultrahigh durability under the operation conditions. The long-term hydrogen evolution reaction catalyzed by $Ru_xSe@MoS_2$ in acidic media was also carried out at a constant current density of -20 mA cm^{-2}. Fig. 4d shows the corresponding time-dependent curve. The potential shows an insignificant variation even after conducting the HER for more than 20 h, further corroborating the supreme stability of

$Ru_xSe@MoS_2$ under acidic conditions. For comparison, we also conducted a long-time HER test for commercial 20% Pt/C catalyst at a same current density. It could be obviously seen from the time-dependent potential curve (Fig. S8, ESI†) that the potential to maintain the same current density various between -60 mV to -130 mV during the long-term HER test, indicating an inferior electrochemical stability of commercial 20% Pt/C catalyst.

3. Conclusions

In summary, we demonstrate a facile two-step hydrothermal method for the decoration of MoS_2 nanosheets with Ru_xSe nanoparticles. Compared with pure MoS_2 and Ru_xSe, the obtained $Ru_xSe@MoS_2$ hybrid exhibits a superior electrocatalytic activity toward HER in both acidic and alkaline media, which could be ascribed to the synergy effect between MoS_2 and Ru_xSe. The synergy effect endows the hybrid catalyst with an enhanced HER kinetics induced by the proliferated active sites and the accelerated charge-transfer process. The outstanding HER performance in basic media could be also related to the bifunctionality of $Ru_xSe@MoS_2$ hybrid, in which Ru promotes

the water adsorption and dissociation to provide intermediate hydrogen, and the nearby Se atoms, unsaturated Mo and/or S atoms act as active sites for the intermediate hydrogen adsorption followed by an electrochemical desorption step to evolve H_2. The facile fabrication and impressive catalytic properties for $Ru_xSe@MoS_2$ make this hybrid a great potential candidate for practical application in electrocatalytic hydrogen evolution reaction. More importantly, our strategy to fabricate highly efficient electrocatalysts based on the low-cost and abundant transitional-metal with the aid of a low usage of noble metal paves a new way for the design of other hybrid systems for electrocatalytic energy conversion.

Conflicts of interest

There are no conflicts to declare.

Acknowledgements

Notes and references

1 G. Zhao, K. Rui, S. X. Dou and W. Sun, *Adv. Funct. Mater.*, 2018, **28**, 1803291.

2 Y. Guo, T. Park, J. W. Yi, J. Henzie, J. Kim, Z. Wang, B. Jiang, Y. Bando, Y. Sugahara, J. Tang and Y. Yamauchi, *Adv. Mater.*, 2019, **31**, 1807134.

3 J. Wang, F. Xu, H. Jin, Y. Chen and Y. Wang, *Adv. Mater.*, 2017, **29**, 1605838.

4 W. Zhong, Z. Lin, S. Feng, D. Wang, S. Shen, Q. Zhang, L. Gu, Z. Wang and B. Fang, *Nanoscale*, 2019, **11**, 4407.

5 Q. Ding, B. Song, P. Xu and S. Jin, *Chem*, 2016, **1**, 699.

6 Y. Shi and B. Zhang, *Chem. Soc. Rev.*, 2016, **45**, 1529.

7 Z. Wu, B. Fang, A. Bonakdarpour, A. Sun, D. P. Wilkinson and D. Wang, *Appl. Catal., B*, 2012, **125**, 59.

8 D. Wang, D. Zhang, C. Tang, P. Zhou, Z. Wu and B. Fang, *Catal. Sci. Technol.*, 2016, **6**, 1952.

9 X. Geng, W. Sun, W. Wu, B. Chen, A. Al-Hilo, M. Benamara, H. Zhu, F. Watanabe, J. Cui and T. P. Chen, *Nat. Commun.*, 2016, **7**, 10672.

10 J. Wang, N. Wang, Y. Guo, J. Yang, J. Wang, F. Wang, J. Sun, H. Xu, Z.-H. Liu and R. Jiang, *ACS Sustainable Chem. Eng.*, 2018, **6**, 13435.

11 Y. Li, M. B. Majewski, S. M. Islam, S. Hao, A. A. Murthy, J. G. DiStefano, E. D. Hanson, Y. Xu, C. Wolverton, M. G. Kanatzidis, M. R. Wasielewski, X. Chen and V. P. Dravid, *Nano Lett.*, 2018, **18**, 7104.

12 Q. Zhang, H. Bai, Q. Zhang, Q. Ma, Y. Li, C. Wan and G. Xi, *Nano Res.*, 2016, **9**, 3038.

13 K. Chang, X. Hai, H. Pang, H. Zhang, L. Shi, G. Liu, H. Liu, G. Zhao, M. Li and J. Ye, *Adv. Mater.*, 2016, **28**, 10033.

14 M. A. R. Anjum, H. Y. Jeong, M. H. Lee, H. S. Shin and J. S. Lee, *Adv. Mater.*, 2018, **30**, 1707105.

15 Z. Wu, C. Tang, P. Zhou, Z. Liu, Y. Xu, D. Wang and B. Fang, *J. Mater. Chem. A*, 2015, **3**, 13050.

16 Z. Wu, B. Fang, Z. Wang, C. Wang, Z. Liu, F. Liu, W. Wang, A. Alfantazi, D. Wang and D. P. Wilkinson, *ACS Catal.*, 2013, **3**, 2101.

17 L. Yang, W. Zhou, J. Lu, D. Hou, Y. Ke, G. Li, Z. Tang, X. Kang and S. Chen, *Nano Energy*, 2016, **22**, 490.

18 J. Xie, H. Zhang, S. Li, R. Wang, X. Sun, M. Zhou, J. Zhou, X. W. Lou and Y. Xie, *Adv. Mater.*, 2013, **25**, 5807.

19 C. Tsai, H. Li, S. Park, J. Park, H. S. Han, J. K. Norskov, X. Zheng and F. Abild-Pedersen, *Nat. Commun.*, 2017, **8**, 15113.

20 T. Sun, J. Wang, X. Chi, Y. Lin, Z. Chen, X. Ling, C. Qiu, Y. Xu, L. Song, W. Chen and C. Su, *ACS Catal.*, 2018, **8**, 7585.

21 S. Wei, X. Cui, Y. Xu, B. Shang, Q. Zhang, L. Gu, X. Fan, L. Zheng, C. Hou, H. Huang, S. Wen and W. Zheng, *ACS Energy Lett.*, 2019, **4**, 368.

22 Y. Cheng, S. Lu, F. Liao, L. Liu, Y. Li and M. Shao, *Adv. Funct. Mater.*, 2017, **27**, 1700359.

23 Y. Shi-Ze, G. Yongji, M. Priyanka, Z. Yu-Yang, Y. Gonglan, C. Shuangming, S. Li, T. P. Sokrates, M. A. Pulickel, F. C. Matthew and Z. Wu, *Adv. Mater.*, 2018, **30**, 1803477.

24 Y. Shi, Y. Zhou, D. R. Yang, W. X. Xu, C. Wang, F. B. Wang, J. J. Xu, X. H. Xia and H. Y. Chen, *J. Am. Chem. Soc.*, 2017, **139**, 15479.

25 Z. Luo, Y. Ouyang, H. Zhang, M. Xiao, J. Ge, Z. Jiang, J. Wang, D. Tang, X. Cao, C. Liu and W. Xing, *Nat. Commun.*, 2018, **9**, 2120.

26 L. X. Chen, Z. W. Chen, Y. Wang, C. C. Yang and Q. Jiang, *ACS Catal.*, 2018, **8**, 8107.

27 Z. Zhao, F. Qin, S. Kasiraju, L. Xie, M. K. Alam, S. Chen, D. Wang, Z. Ren, Z. Wang, L. C. Grabow and J. Bao, *ACS Catal.*, 2017, **7**, 7312.

28 S. Park, J. Park, H. Abroshan, L. Zhang, J. K. Kim, J. Zhang, J. Guo, S. Siahrostami and X. Zheng, *ACS Energy Lett.*, 2018, **3**, 2685.

29 Y. Luo, X. Li, X. Cai, X. Zou, F. Kang, H. M. Cheng and B. Liu, *ACS Nano*, 2018, **12**, 4565.

30 X. Zhang and Y. Liang, *Adv. Sci.*, 2018, **5**, 1700644.

31 H. Zhang, L. Yu, T. Chen, W. Zhou and X. W. Lou, *Adv. Funct. Mater.*, 2018, **28**, 1807086.

32 M. Kim, M. A. R. Anjum, M. Lee, B. J. Lee and J. S. Lee, *Adv. Funct. Mater.*, 2019, **29**, 1809151.

33 J. Zhang, T. Wang, P. Liu, S. Liu, R. Dong, X. Zhuang, M. Chen and X. Feng, *Energy Environ. Sci.*, 2016, **9**, 2789.

34 J. Liu, J. Wang, B. Zhang, Y. Ruan, H. Wan, X. Ji, K. Xu, D. Zha, L. Miao and J. Jiang, *J. Mater. Chem. A*, 2018, **6**, 2067.

35 B. Zhang, J. Liu, J. Wang, Y. Ruan, X. Ji, K. Xu, C. Chen, H. Wan, L. Miao and J. Jiang, *Nano Energy*, 2017, **37**, 74.

36 M. Watanabe and S. Motoo, *J. Electroanal. Chem. Interfacial Electrochem.*, 1975, **60**, 267.

37 D. J. Chen and Y. J. Tong, *Angew. Chem., Int. Ed. Engl.*, 2015, **54**, 9394.

38 D. Strmcnik, P. P. Lopes, B. Genorio, V. R. Stamenkovic and N. M. Markovic, *Nano Energy*, 2016, **29**, 29.

39 R. Ge, S. Wang, J. Su, Y. Dong, Y. Lin, Q. Zhang and L. Chen, *Nanoscale*, 2018, **10**, 13930.

40 Y. Wang, Z. Liu, H. Liu, N. T. Suen, X. Yu and L. Feng, *ChemSusChem*, 2018, **11**, 1.

41 T. Liu, S. Wang, Q. Zhang, L. Chen, W. Hu and C. M. Li, *Chem. Commun.*, 2018, **54**, 3343.

42 J. Q. Chi, W. K. Gao, J. H. Lin, B. Dong, K. L. Yan, J. F. Qin, B. Liu, Y. M. Chai and C. G. Liu, *ChemSusChem*, 2018, **11**, 743.

43 Z. Pu, I. S. Amiinu, Z. Kou, W. Li and S. Mu, *Angew. Chem., Int. Ed.*, 2017, **56**, 11559.

44 J. Yu, Y. Guo, S. She, S. Miao, M. Ni, W. Zhou, M. Liu and Z. Shao, *Adv. Mater.*, 2018, **30**, 1800047.

45 T. Liu, B. Feng, X. Wu, Y. Niu, W. Hu and C. M. Li, *ACS Appl. Energy Mater.*, 2018, **1**, 3143.

46 W. Li, Y. Liu, M. Wu, X. Feng, S. A. T. Redfern, Y. Shang, X. Yong, T. Feng, K. Wu, Z. Liu, B. Li, Z. Chen, J. S. Tse, S. Lu and B. Yang, *Adv. Mater.*, 2018, **30**, 1800676.

47 J. Zhang, P. Liu, G. Wang, P. P. Zhang, X. D. Zhuang, M. W. Chen, I. M. Weidinger and X. L. Feng, *J. Mater. Chem. A*, 2017, **5**, 25314.

48 B. K. Barman, D. Das and K. K. Nanda, *Sustainable Energy Fuels*, 2017, **1**, 1028.

49 J. Ohyama, D. Kumada and A. Satsuma, *J. Mater. Chem. A*, 2016, **4**, 15980.

50 Q. Wang, M. Ming, S. Niu, Y. Zhang, G. Fan and J.-S. Hu, *Adv. Energy Mater.*, 2018, **9**, 1801698.

51 R. Ye, Y. Liu, Z. Peng, T. Wang, A. S. Jalilov, B. I. Yakobson, S. H. Wei and J. M. Tour, *ACS Appl. Mater. Interfaces*, 2017, **9**, 3785.

52 F. Li, G. F. Han, H. J. Noh, I. Ahmad, I. Y. Jeon and J. B. Baek, *Adv. Mater.*, 2018, **30**, 1803676.

53 X. Cheng, H. Wang, M. Ming, W. Luo, Y. Wang, Y. Yang, Y. Zhang, D. Gao, J. Bi and G. Fan, *ACS Sustainable Chem. Eng.*, 2018, **6**, 11487.

54 Y. Zheng, Y. Jiao, Y. Zhu, L. H. Li, Y. Han, Y. Chen, M. Jaroniec and S. Z. Qiao, *J. Am. Chem. Soc.*, 2016, **138**, 16174.

55 J. Mahmood, F. Li, S. M. Jung, M. S. Okyay, I. Ahmad, S. J. Kim, N. Park, H. Y. Jeong and J. B. Baek, *Nat. Nanotechnol.*, 2017, **12**, 441.

56 J. Yu, Y. Guo, S. Miao, M. Ni, W. Zhou and Z. Shao, *ACS Appl. Mater. Interfaces*, 2018, **10**, 34098.

57 S. Liu, Q. Liu, Y. Lv, B. Chen, Q. Zhou, L. Wang, Q. Zheng, C. Che and C. Chen, *Chem. Commun.*, 2017, **53**, 13153.

58 J. Liu, Y. Zheng, D. Zhu, A. Vasileff, T. Ling and S. Z. Qiao, *Nanoscale*, 2017, **9**, 16616.

59 K. Yang, P. Xu, Z. Lin, Y. Yang, P. Jiang, C. Wang, S. Liu, S. Gong, L. Hu and Q. Chen, *Small*, 2018, **14**, 1803009.

60 J. Xu, T. Liu, J. Li, B. Li, Y. Liu, B. Zhang, D. Xiong, I. Amorim, W. Li and L. Liu, *Energy Environ. Sci.*, 2018, **11**, 1819.

61 S. Anantharaj, S. R. Ede, K. Sakthikumar, K. Karthick, S. Mishra and S. Kundu, *ACS Catal.*, 2016, **6**, 8069.

62 Y. Liu, S. Shen, J. Zhang, W. Zhong and X. Huang, *Appl. Surf. Sci.*, 2019, **478**, 762.

63 W. Zhong, S. Shen, S. Feng, Z. Lin, Z. Wang and B. Fang, *CrystEngComm*, 2018, **20**, 7851.

64 W. Zhong, W. Tu, S. Feng and A. Xu, *J. Alloys Compd.*, 2019, **772**, 669.

65 F. Wang, Y. Li, T. A. Shifa, K. Liu, F. Wang, Z. Wang, P. Xu, Q. Wang and J. He, *Angew. Chem., Int. Ed.*, 2016, **55**, 6919.

66 H. Zhou, F. Yu, Y. Liu, J. Sun, Z. Zhu, R. He, J. Bao, W. A. Goddard, S. Chen and Z. Ren, *Energy Environ. Sci.*, 2017, **10**, 1487.

67 K. Wang, Q. Chen, Y. Hu, W. Wei, S. Wang, Q. Shen and P. Qu, *Small*, 2018, **14**, 1802132.

68 J. Deng, H. Li, J. Xiao, Y. Tu, D. Deng, H. Yang, H. Tian, J. Li, P. Ren and X. Bao, *Energy Environ. Sci.*, 2015, **8**, 1594.

69 Q. Liu, X. Li, Q. He, A. Khalil, D. Liu, T. Xiang, X. Wu and L. Song, *Small*, 2015, **11**, 5556.

70 H. Wang, Z. Lu, D. Kong, J. Sun, T. M. Hymel and Y. Cui, *ACS Nano*, 2014, **8**, 4940.